



Optimization of Segmented Thermal Barrier Coatings (s-TBCs) for High-Temperature Applications

Behiye Aybike Yalçınüz^{1,3} · Franz Kamutzki² · Aleksander Gurlo² · Christian Rupprecht¹

Submitted: 22 August 2022 / in revised form: 17 July 2023 / Accepted: 13 August 2023 / Published online: 29 August 2023
© The Author(s) 2023

Abstract Hot section components of stationary gas turbines, such as turbine blades and vanes, are coated with thermal barrier coatings (TBCs) to increase the component life. TBCs provide thermal insulation to the metallic components from hot gas in the gas turbines. The TBCs represent high-performance ceramics and are mainly composed of yttria-stabilized zirconia (YSZ) to fulfill the thermal insulation function. The microstructure of the TBCs should be porous to decrease heat conduction. Besides the porous TBCs, the subsequently developed vertically segmented thermal barrier coatings (s-TBCs) feature outstanding thermal durability. For the formation of this segmented coating microstructure, the YSZ should be deposited under high thermal tensile stress during the coating process. Therefore, substrates are heated just

before the coating by plasma or in an oven in recent research. In this work, the development of process parameters for s-TBCs produced by atmospheric plasma spray (APS) without pre-heating is presented. Within the experiments, the relevant process parameters, such as plasma gases, powder feed rate, surface speed, and pathway strategy, have been optimized to achieve the segmented coating microstructure with high deposition efficiency by a conventional plasma torch. Furthermore, YSZ powders used in this study are characterized, and the effect of powder characteristics on the coating microstructure is investigated. The coating microstructure in this work aims to achieve the formation of a high number of vertical cracks with a combination of low internal residual stress and high adhesive tensile strength for the s-TBCs.

This article is an invited paper selected from presentations at the 2022 International Thermal Spray Conference, held May 4–6, 2022, in Vienna, Austria, and has been expanded from the original presentation. The issue was organized by André McDonald, University of Alberta (Lead Editor); Yuk-Chiu Lau, General Electric Power; Fardad Azarmi, North Dakota State University; Filofteia-Laura Toma, Fraunhofer Institute for Material and Beam Technology; Heli Koivuluoto, Tampere University; Jan Cizek, Institute of Plasma Physics, Czech Academy of Sciences; Emine Bakan, Forschungszentrum Jülich GmbH; Šárka Houdková, University of West Bohemia; and Hua Li, Ningbo Institute of Materials Technology and Engineering, CAS.

✉ Behiye Aybike Yalçınüz
aybike.yalcinyuez@ipk.fraunhofer.de

¹ Chair of Coating Technology, Technische Universität Berlin, Berlin, Germany

² Chair of Advanced Ceramic Materials, Technische Universität Berlin, Berlin, Germany

³ Fraunhofer Institute for Production Systems and Design Technology IPK, Pascalstraße 8 – 9, 10587 Berlin, Germany

Keywords atmospheric plasma spraying (APS) · deposition efficiency (DE) · gas turbine blades · powder characterization · segmented thermal barrier coatings (s-TBCs) · yttria-stabilized zirconia (YSZ)

Introduction

Thermal barrier coatings (TBCs) are multilayer protective coatings that are applied to hot section components of stationary gas turbines to decrease component temperatures and hence increase component life. A typical application of the TBCs is on turbine blades and vanes, which consist of a metallic bond coat and a ceramic topcoat on a Ni-superalloy substrate (Ref 1, 2).

The bond coat is a metallic layer MCrAlY (M=Ni, Co, or NiCo) to protect the Ni-superalloy substrate from oxidation and corrosion and to enhance the adhesion between

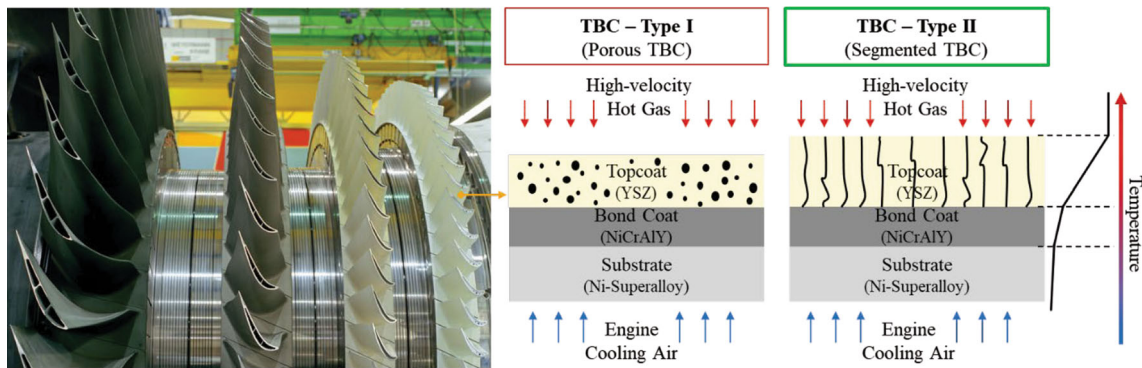


Fig. 1 Schematic illustration of thermal barrier coating (TBC) types for a gas turbine blade. Photograph provided by Siemens Energy (Ref 11). Illustration based on (Ref 1)

the ceramic topcoat and the substrate. The ceramic topcoat provides thermal insulation with low thermal conductivity and is generally used yttria-stabilized zirconia (YSZ). The YSZ is also chemically resistant to hot gas atmospheres and has high thermal stability with a compatible thermal expansion coefficient. In the industry, the 6–8 wt.% yttria-stabilized zirconia (7YSZ) has become a standard topcoat because of its high-temperature durability, compared with lower and higher than 6–8 wt.% yttria contents (Ref 2–4).

The YSZ topcoat can be deposited using atmospheric plasma spray (APS) or electron beam physical vapor deposition (EB-PVD) process. The atmospheric plasma-sprayed coatings are notable with thermal conductivity, while the EB-PVD coatings have low surface roughness with high thermal shock resistance. The coating process should be chosen according to the applications and requirements of the target field. However, the APS process is preferable in the fields of aerospace and power generation gas turbines because of its ability to coat larger and more complicated forms at a lower cost and higher deposition rate (Ref 4–6).

The thermal conductivity of the dense 7YSZ is ca. 2.3 W/m K at 1000 °C. On the other hand, the thermal conductivity of the 7YSZ topcoat can be decreased due to its microstructure by the different coatings processes, such as by EB-PVD 1.5–1.9 W/m K (columnar microstructure) and by APS 0.8–1.1 W/m K (micro-cracked, porous microstructure). Furthermore, the strain tolerance of the TBCs increases with the help of the columnar microstructures and thus improves the thermal shock behaviors as well as thermal cycling performance, as compared with the porous microstructure. Therefore, the segmented thermal barrier coatings (s-TBCs) have been developed with the combination of the benefits of these two microstructures by APS in recent years (Ref 1, 7–9).

The operating temperature of gas turbines can reach 1500 °C through combustion gases. The function of the

TBC system is the reduction of the component temperature, relative to component surfaces that are exposed to combustion gases (Ref 1, 4). Through vertical cracks on the segmented coating microstructure, s-TBCs resist stronger strains, caused by the coefficient of thermal expansion mismatch between the YSZ topcoat and the metallic bond coat, compared to porous TBC (Ref 10). The mechanism by which TBCs of two types (porous and segmented) reduce component surface temperature is schematically illustrated in Fig. 1.

The first investigation about the formation of vertical cracks was patented by Taylor (Ref 12) in 1991 and explained that, in principle, the segmented microstructure is relevant with a temperature gradient between well-bonded splats and higher coating surface temperatures. During the solidification of liquid splats, the recently sprayed hot liquid splats remelt the surface of the underlying splats and they can shrink more than the underlying splats. In this way, the vertical cracks build-up due to biaxial tensile stresses within individual splats (Ref 12, 13).

Studies by Guo et al. (Ref 14) remarked the heat input into the powder feedstock material, and the substrate must be controlled for the formation of vertical cracks during the APS process. Thus, the thermal tensile stress required for the segmentation microstructure can occur. This heat input is controllable by spray distance, air pressure from two air jets, the velocity of the plasma gun, and powder feed rate. This is also reported by the study of Karger et al. (Ref 15), which considers the maximization of the temperature gradient with APS process parameters for instance high material feed rate and/or lower velocity of plasma gun during layer-by-layer deposition.

Recent studies by Shinde (Ref 13) investigated the mechanism of segmentation cracks. Initially, high surface temperatures for the formation of segmentation microstructure are supported by their in situ stress measurement method. For porous TBCs (Type I), layer-by-

Table 1 Powder composition and manufacturing process of Metco 204F and Amperit 825 (Ref 16, 17)

Feedstock powder	Metco 204F	Amperit 825
Powder composition [in wt.%]	ZrO ₂ /8Y ₂ O ₃	ZrO ₂ /7Y ₂ O ₃
Manufacturing process	Agglomerated & hollow spherical powder (HOSP)	Fused & crushed
Particle size distribution	– 44 + 16 μm	– 60 + 25 μm
Powder morphology	Spheroidal	Angular
Crystallite size	64.5 nm	46.1 nm

layer deposition results in a low and almost constant level of stress in the deposit. On the other hand, two steps under deposition circumstances would encourage the formation of segmentation cracks (Type II): First, a large amount of stress is generated, which is then flattened as the strain is relieved by the development of segmentation fractures in subsequent layers.

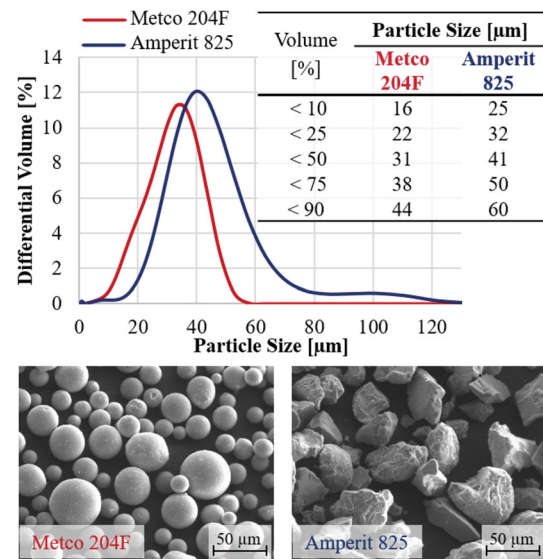
As other studies about s-TBCs showed, a higher substrate or coating deposition temperature caused a transformation from splat microcracking to large macroscale cracking (vertical cracks). Therefore, substrates are pre-heated just before the coating by plasma plume to achieve high thermal stress in recent studies (Ref 7, 15). Moreover, the thermal cycling resistance of s-TBCs (Type II) is more than that of the conventional porous TBCs (Type I), as studied by Guo et al. (Ref 8), Karger et al. (Ref 15) and Chen et al. (Ref 10).

In this study, the segmented thermal barrier coatings (s-TBCs) are deposited without pre-heated. The required high deposition temperature is constituted by the process parameters. The deposition temperature can be adjusted with a high plasma enthalpy, a short spray distance, or a pathway strategy. To optimize the s-TBCs by APS, the process parameters are researched in this study by organizing them into three parameter groups:

- Feedstock powder parameter (powder characteristic, powder feed rate)
- Plasma parameter (plasma power, plasma gases ratio)
- Robot movement parameters (spray distance, surface speed, scanning step)

Experimental Methods

All samples are coated using an F6-Plasma Torch with a 6-mm nozzle [GTV Verschleißschutz GmbH, Germany] mounted on a 6-axis robot KR16-2 [KUKA GmbH, Germany] in the GTV-Plasma system for atmospheric plasma spraying (APS) where located at the Institute for Machine Tools and Factory Management (IWF) in Berlin, Germany. Argon and hydrogen are used as primary and secondary plasma gases, respectively. The coatings are deposited onto sandblasted non-alloy steel (EN 1.0038) substrates

**Fig. 2** Particle size distribution and powder morphology of Metco 204F and Amperit 825

(100mm × 80mm × 10mm) with YSZ powders, which are conventionally used for the topcoat of the gas turbine blades.

Feedstock Powder

Yttria-stabilized zirconia (YSZ) feedstock powders from two different manufacturers are used in this study to achieve the segmented microstructure: Metco 204F [Oerlikon Metco, Switzerland] and based on Amperit 825 [Höganäs, Sweden]. The differences between these powders are presented in Table 1 and Fig. 2, such as the manufacturing process, powder composition, particle size distribution, and powder morphology.

The particle size distribution of sample powders is determined in de-ionized water-dispersed form using the Universal Liquid Module (ULM) of an LS13320 laser diffraction particle size analyzer [Beckman Coulter, USA]. The powder morphology is examined by a scanning electron microscope (SEM) Hitachi S-520 [Hitachi Ltd., Japan]. The Metco 204F powder has a volume-proportion-based particle size of d10% = 16 μm, d50% = 31 μm, and d90% = 44 μm. On the other hand, the powder particle size of Amperit 825 is coarser than Metco 204F, with particle

sizes of $d_{10\%} = 25 \mu\text{m}$, $d_{50\%} = 41 \mu\text{m}$, and $d_{90\%} = 60 \mu\text{m}$. Due to the different manufacturing processes of the feedstock powders, the powder morphology of Metco 204F is spheroidal (hollow spherical powder), whereas the morphology of Amperit 825 is angular.

The phase analysis of the YSZ feedstock powders is carried out with a D8 ADVANCE x-ray diffractometer (XRD) in Bragg–Brentano geometry [Bruker, USA], equipped with a LynxEye detector and Cu radiation ($\lambda = 1.5406 \text{ \AA}$). Crystallite sizes are calculated according to Scherrer's method (Ref 18). The XRD patterns for the feedstock powders are shown in Fig. 3. The peaks of the YSZ-T' phase (called non-transformable tetragonal), YSZ-cubic phase and a slight amount of YSZ-monoclinic phase, are identified in both powders. The peaks of Metco 204F powder are shown similarly in the studies by Ilavsky et al. (Ref 19) within the scope of HOSP powder.

It is difficult to discriminate between tetragonal and cubic diffractograms of 8YSZ. Both show lattice structures with the same spacing, and thereby, they are located at the same position in the diffractogram (Ref 20). On the other hand, the studies of Zhang et al. (Ref 21) and Mao et al. (Ref 22) are shown that the amount of cubic phase is increased with more yttria contents and the form of their main peaks at ca. 30° and 50° gets higher angle. This higher angle of the main peaks can be seen also at Amperit 825, although the content of yttrium for Amperit 825 (7%) is lower than Metco 204F (8%). The amount of phases of fused-crushed and HOSP powders was analyzed in the study of Ilavsky et al. (Ref 19) and was shown that the cubic phase in mass is 26% in HOSP and 40% in fused-crushed powder, respectively. These differences in phase contents can be explained by the different powder manufacturing processes.

In conclusion, the shape of the peaks for Amperit 825 powder is at a higher angle than that of Metco 204F

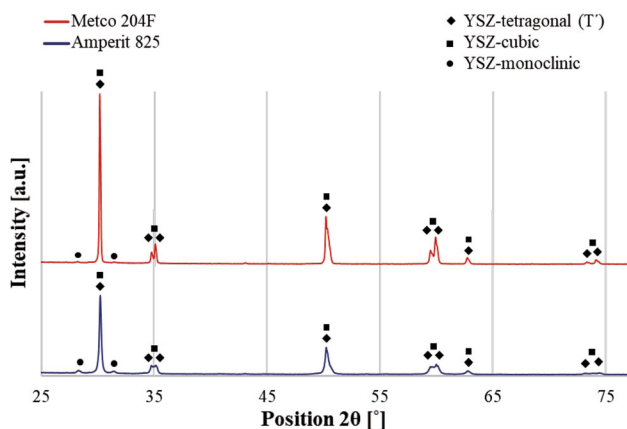


Fig. 3 XRD patterns of feedstock powders for Metco 204 and Amperit 825

powder. The reason can be attributed to the presence of a likely higher amount of cubic phase for Amperit 825 than Metco 204F. Furthermore, the crystallite size (cs) of Amperit 825 (46.1 nm) is smaller than Metco 204F (64.5 nm).

Spray Process Parameters

During the APS process, the plasma gases (Ar and H_2) mixture is ionized and generates a plasma jet with high energy. Thus, the plasma energy reaches the melting point of the feedstock material to melt it, e.g., the melting point of pure zirconia is 2690°C . The ratio of the plasma gases influences the degree of melting of the sprayed particles, as well as the deposition efficiency (Ref 2, 23). Figure 4 provides the schematic illustration of the APS process and their reliable process parameter in this study.

Before the experiments of the segmented thermal barrier coatings (s-TBCs) are carried out, the deposition efficiency for 7YSZ powders should be initially optimized by adjusting the plasma and the powder parameters.

For this, different amounts of powders are sprayed on the substrate at a certain time with different plasma parameters. This experiment is called “spray spot deposition,” as shown in Fig. 4. Then, the difference in the weight of the sample before and after deposition is measured (weight of spray spot). The deposition efficiency (DE) is calculated afterward by using the following equation. The spray process parameters for the optimization of the deposition efficiency for both powders, Metco 204F and Amperit 825, are shown in Table 2.

$$\text{Deposition Efficiency (DE)} = \frac{\text{Weight of spray spot}}{\text{Powder feed rate} \times \text{Process time}} \times 100$$

According to the results of the spray spot deposition experiments, the ratio of plasma gases is defined. Since the coating deposition temperature has a significant effect on the formation of the vertical cracks on the TBCs microstructures, the plasma power should be high, and the spray distance should be as low as possible according to the GTV-Plasma system. Moreover, it was determined by preliminary experiments that the scanning step should be bigger than 3 mm and the surface speed should be faster than 400 mm/s at the same condition of the plasma parameter. Otherwise, it could cause coating spallation and coating delamination due to very high thermal tensile stress during deposition as shown in Fig. 5. The samples are deposited with a coating thickness of around 500–600 μm , and the number of passes is adjusted accordingly. The constant and variable spray process parameters for the optimization of the microstructure of segmented barrier coatings (s-TBCs) are shown in Table 3. Furthermore, the deposition efficiency of coatings is calculated by the

Fig. 4 Schematic illustration of APS process in this study

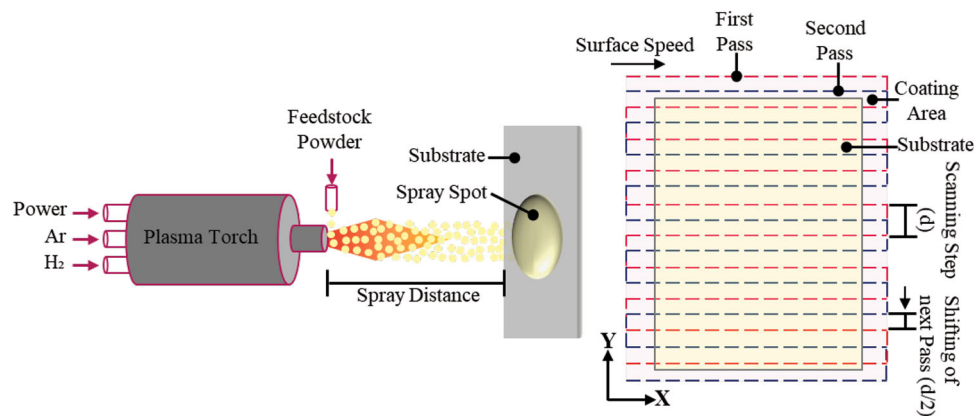


Table 2 Spray process parameters for the optimization of the deposition efficiency

Power	Process time	Spray distance	Powder feed rate	Carrier gas: Ar	Primary plasma gas: Ar	Secondary plasma gas: H ₂
≈ 40 kW	10 s	75 mm	30-50 g/min	2 slpm	30-40 slpm	8-12 slpm

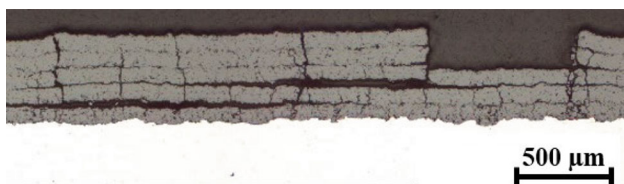


Fig. 5 Coating spallation and delamination

determination of the process time on the substrate with the robot movement parameter. The process time on the substrate is related to the surface speed and the step size. When the surface speed is faster and the step size is bigger, the deposition is running also faster, thereby the coating is thinner, sort of less amount of deposition.

Deposition Efficiency (DE)

$$= \frac{\text{Weight of coating}}{\text{Powder feed rate} \times \text{Process time on substrate}} \times 100$$

Microstructural Characterization

After the deposition of the coatings, the samples are embedded, ground, and polished using standard metallographic equipment to analyze the coating microstructures. Subsequently, the coating microstructures are characterized using an optical light microscopy Zeiss AxioImager.A2m with the software Zeiss ZEN Core v3.2 [Carl Zeiss AG, Germany] and the SEM Hitachi S-520. The microstructural properties are defined as follows (Ref 24):

- Segmentation cracks (vertical cracks): cracks running perpendicular to the coating surface and penetrating longer than three quarters (3/4) of the coating thickness
- Branching cracks (horizontal cracks): cracks parallel to the coating plane on the segmentation cracks
- Coating deposition efficiency: ratio of coating weight to the weight of the total feedstock

Segmentation crack density, which is one of the significant coating properties for s-TBCs, is calculated by the following equation:

$$\text{Crack Density (CD)} = \frac{\text{Number of vertical cracks}}{\text{Cross-section length}}$$

Experimental Results

Optimization of Deposition Efficiency

The first experiments are carried out with only Metco 204F powders and with a high ratio of plasma gases, for instance, Ar/H₂: ≈ 3.3-5. Thereby, the deposition efficiency reaches the maximum of ca. 40%. Then, the ratio of plasma gases is reduced through the increase of H₂ and the decrease of Ar, Ar/H₂: < 3, and applied on Metco 204F and Amperit 825. When the ratio of argon hydrogen gases is 2.5 (Ar/H₂:30/12 slpm), the deposition efficiency of Metco204F enhances above 50%, whereas that of Amperit 825 is above 60%. Although the powder particle size of Metco 204F is finer than Amperit 825, the fused and crushed particles (Amperit 825) melted in more quantity than hollow spherical

Table 3 Spray process parameters for the optimization of the s-TBCs microstructure

Power	Plasma gas ratio	Spray distance	Powder feed rate	Carrier gas: Ar	Surface speed	Scanning step
≈ 40 kW	30/12 slpm	75 mm	30-50 g/min	2 slpm	400-500 mm/s	3-5 mm

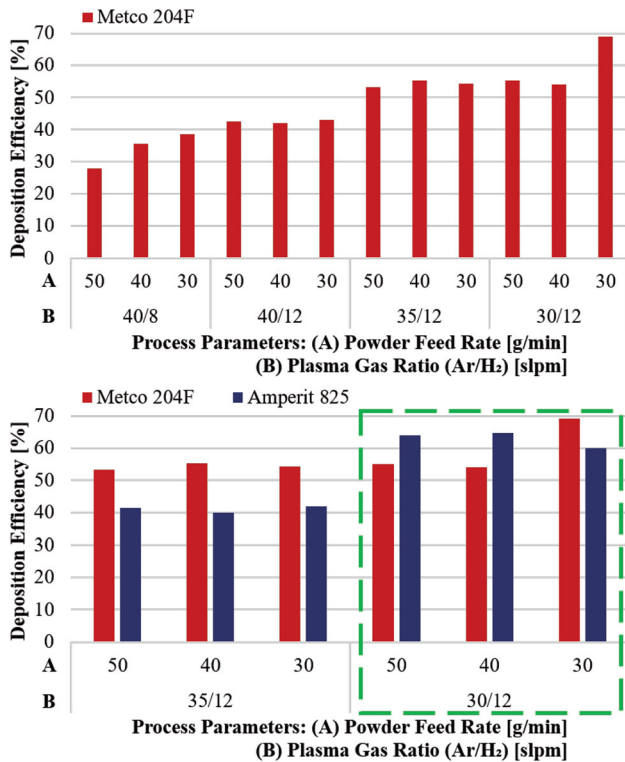


Fig. 6 Effect of process parameters on deposition efficiency for Metco 204F and Amperit 825

particles (Metco 204F) at the same plasma conditions (Ar/H₂:30/12 slpm). However, there is a 1% yttrium difference in weight between Metco 204F (8%) and Amperit 825 (7%). Moreover, the powder feed rate has a slight effect on the lower gas ratio, especially for Amperit 825. Figure 6 demonstrates the deposition efficiency for both powders depending on the process parameters such as the powder feed rate and the plasma gas ratio.

Optimization of Segmented Thermal Barrier Coatings (s-TBCs)

With the aim of the analyzing effect of the process parameters on the segmented thermal barrier coatings (s-TBCs), such as the powder feed rate, the surface speed, and the scanning step, the respective experiments are carried out in this study. As a beginning, the fused and crushed powders (Amperit 825) are used in the s-TBCs experiments due to their high deposition rate. Then, the chosen

experiment runs are applied with the hollow spherical powder (Metco 204F) to compare the effect of the different powder types. The spray process parameters of the experimental plan for Amperit 825 and Metco 204F and their results regarding the coating deposition efficiency (DE), the coating thickness (CT), and the cracks density (CD) are shown in Table 4.

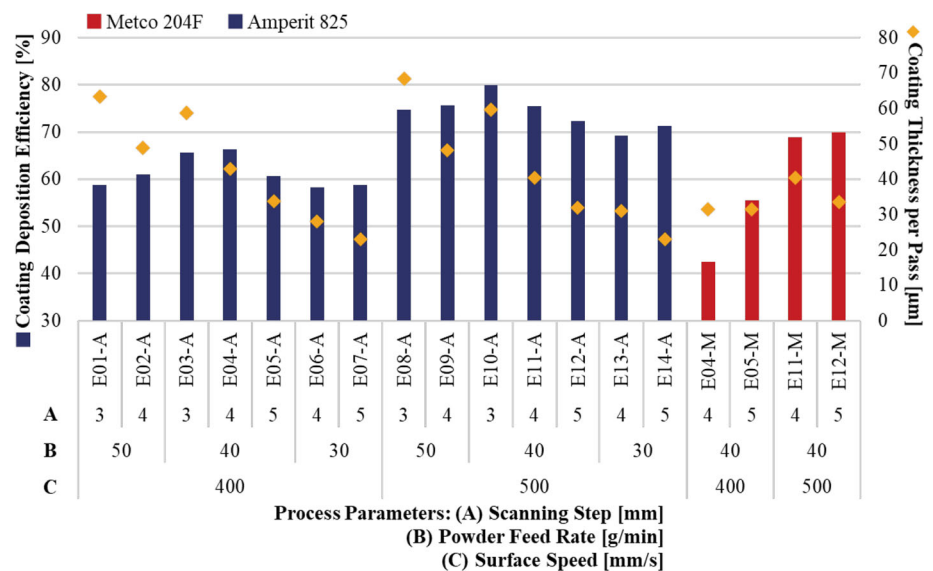
Figure 7 provides an illustration of the correlation between the coating deposition efficiency and the coating thickness per pass according to the different spray process parameters. As illustrated by the graph, the deposition efficiency increases above 70% with a surface speed of 500 mm/s for the fused and crushed powders. Although the deposition efficiency is higher than 70% at 500 mm/s, the coating thickness per pass is identical to the ones obtained with 400 mm/s same properties otherwise, such as the scanning step and powder feed rate. The same effect of the surface speed can be also seen on the hollow spherical powders. Generally, it is expected that the coating thickness could be decreased with the higher surface speed or the bigger scanning step. Thus, the process runs faster as well as the process time is shorter. However, the coating thickness or the coating thickness per pass remains relatively identical at the surface speed of 400 and 500 mm/s, since the coating efficiency increases with the higher surface speed in these experiments.

On the other hand, the scanning step has an efficient influence on the coating thickness per pass. Furthermore, the comparison of the segmented coating microstructures, which are deposited with different surface speeds and different scanning steps, is shown in Fig. 8. As can be seen in Fig. 8, different surface speed results are in similar microstructure, at each scanning step of 3, 4, and 5 mm, respectively, e.g., E03-A and E10-A, E04-A and E11-A, or E05-A and E12-A. For instance, the pores and the branching cracks at the interface between two passes can be visible on the scanning step of 3 mm with a surface speed of either 400 or 500 mm/s (E03-A and E10-A). On the contrary, these pores or these horizontal cracks become less with increasing scanning steps (E05-A and E12-A).

Figure 9 demonstrates the coating microstructure deposited with different powder feed rates, such as 50, 40, and 30 mm/s, respectively. A similar effect of the less amount of pores and the shorter horizontal cracks at the interface between two passes can be also determined on

Table 4 Spray process parameters of experimental plan for feedstock powder of Amperit 825 (A) and Metco 204F (M)

Experiment no.	Surface speed, mm/s	Scanning step, mm	Powder feed rate, g/min	Coating DE, %	CT, μm	CT per pass, μm	CD, mm^{-1}
E01-A	400	3	50	59	569 \pm 12	63	2.0
E02-A	400	4	50	61	538 \pm 10	49	2.4
E03-A	400	3	40	66	529 \pm 10	59	2.4
E04-A	400	4	40	66	473 \pm 13	43	2.6
E05-A	400	5	40	61	505 \pm 17	34	2.4
E06-A	400	4	30	58	419 \pm 9	28	1.6
E07-A	400	5	30	59	347 \pm 9	23	1.4
E08-A	500	3	50	75	751 \pm 21	68	2.4
E09-A	500	4	50	76	676 \pm 6	48	2.0
E10-A	500	3	40	80	657 \pm 9	60	1.8
E11-A	500	4	40	75	485 \pm 16	40	2.4
E12-A	500	5	40	72	480 \pm 11	32	2.0
E13-A	500	4	30	69	464 \pm 9	31	1.2
E14-A	500	5	30	71	345 \pm 11	23	1.6
E04-M	400	4	40	45	471 \pm 11	31	2.6
E05-M	400	5	40	56	473 \pm 14	32	2.2
E11-M	500	4	40	69	606 \pm 7	40	2.4
E12-M	500	5	40	70	502 \pm 19	33	2.6

Fig. 7 Effect of process parameters on coating deposition efficiency and coating thickness per pass

these microstructures when the process runs with less powder amount. Furthermore, the length of vertical cracks is shorter than three quarters of the coating thickness and not 90° perpendicular, while the crack density is less at the powder feed rate of 30 g/min (1.6 mm^{-1}), compared to 40 g/min (2.6 mm^{-1}) or 50 g/min (2.4 mm^{-1}).

Subsequently, the experimental series “E04, E05, E11, and E12,” which are suitable for the segmentation with fused and crushed powders, are applied with the hollow spherical powder (Metco 204F). The coating microstructures of these comparison experiments with HOSP are

depicted in Fig. 10. The vertical cracks can also occur with the process parameters of these experimental series for Metco 204F. However, it can be defined as longer branching cracks and a higher amount of porous at the interface between two passes on the microstructures compared to Amperit 825 experiments.

Another remarkable result to analyze for s-TBCs is the crack density. Figure 11 illustrates the vertical crack density of the experiments for Amperit 825 and Metco 204F. The crack density of the experiments with Amperit 825 is more than 2 mm^{-1} , except for E06-A, E07-A, E13-A, and

Fig. 8 Effect of scanning step and surface speed on segmented coating microstructure for Amperit 825: powder feed rate: 40 g/min, surface speed: 400 and 500 mm/s (left to right), scanning step: 3, 4, and 5mm (top to bottom)

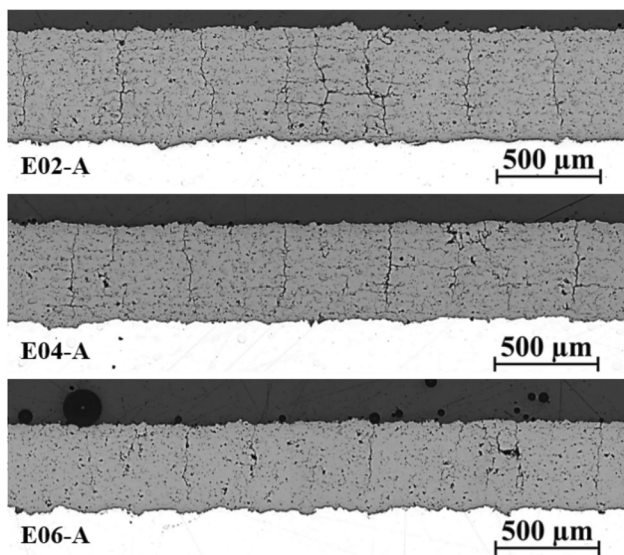
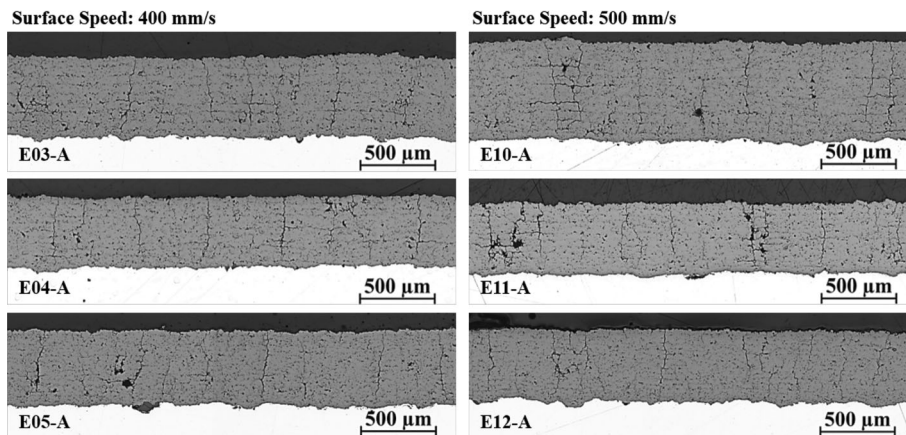


Fig. 9 Effect of powder feed rate on segmented coating microstructure for Amperit 825: surface speed: 400 mm/s, scanning step: 4mm, powder feed rate: 50, 40, and 30 g/min (top to bottom)

E14-A, which are deposited with the powder feed rate of 30 g/min. Although the vertical crack density is over ca. 2-2.5 mm⁻¹ with Metco 204F, their coating microstructure does not fulfil, especially due to the longer horizontal cracks.

Discussion

The results presented in this study indicate the effects of the spray process parameters and the powder characteristic on the production of the segmented thermal barrier coatings. The marked difference between this study and literature studies is that these experiments are carried out without pre-heating and the required thermal tensile stress is optimized with the process parameters. Literature studies about this topic are summarized in Table 5.

As presented in Table 5, the feedstock powder characteristics and the plasma torch type (1 anode + 1 cathode or

3 anodes + 1 cathode) are significant components of the APS system for the formation of the segmented structure. The hollow spherical powder (HOSP) is the most used powder type in past studies, and the problem of longer horizontal cracks can be seen also in these studies. However, Chen (Ref 7) solved this problem by decreasing the coating thickness per pass (from 40 to 20 μm) while increasing the plasma power (from 52 to 74 kW). Thus, the length of these horizontal cracks decreases from approximately 1000 to 180 μm with a crack density of 2.5 mm⁻¹. In accordance with Guo (Ref 8), the segmentation cracks occur at 700 °C with the solid powder and 850 °C with the hollow powder.

In substance, the main point of the segmented crack formation is the deposition of powder amount per pass according to these experiments between E01-A and E14-A. When the coating thickness per pass is thinner than ca. 30 μm, the form of the vertical cracks is undesirable, such as E06-A. The required vertical cracks should be longer than 3/4 of the coating thickness, so when the pass thickness exceeds 30 μm, the desired length is reached, for instance, E03-A, E04-A as well as E05-A. However, when one pass is thicker than ca. 50 μm such as E01-A, E02-A, and E03-A, the longer branching (horizontal) cracks occur on the vertical cracks and the pores arise between each pass, which causes the delamination of the coatings. Consequently, the coating thickness per pass should be between 35 and 45 μm for the fused and crushed powders to achieve the optimized segmented cracks in this study. The coating thickness per pass is adjusted by the spray process parameter as well as the pathway strategy and the powder feed rate. The effect of coating thickness per pass on the segmented microstructure for experiments with Amperit 825 is illustrated in Fig. 12.

Another important conclusion to be drawn from this study is that the powder type has a significant effect on the microstructure, as shown in Fig. 13. As a result of experiments with the fused and crushed powders, the E04-A has

Fig. 10 Effect of scanning step and surface speed on segmented coating microstructure for Metco 204F: powder feed rate: 40 g/min, surface speed: 400 and 500 mm/s (left to right), scanning step: 4 and 5 mm (top to bottom)

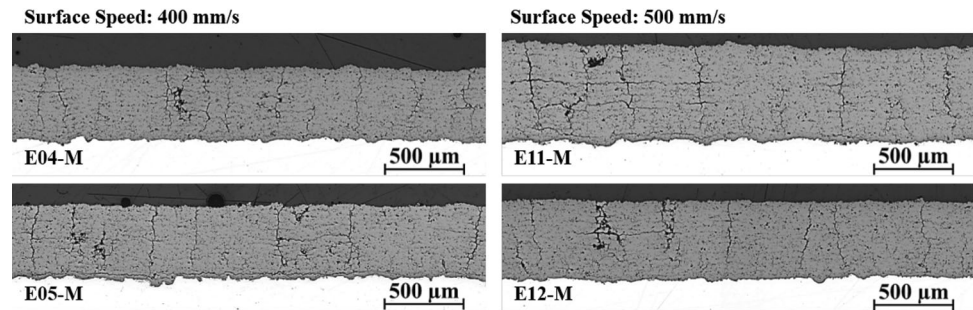


Table 5 Literature studies about segmented thermal barrier coatings (s-TBCs)

Reference	Feedstock powder				
	Industry name	Powder morphology	Particle size, μm	Plasma torch	Pre-treatment
Guo [2004-2006] (Ref 8, 14)	Metco 204NS	Hollow powder	– 20 + 120	Metco-Triplex	Pre-heated with plasma
	Showa Denko K-90	Solid angular powder	– 10 + 60	Praxair-SG100	
Karger [2011] (Ref 15)	Treibacher AG	Fused & crushed	– 9 + 51	Metco Triplex II (9 mm)	Pre-heated upto 500 °C with plasma
Chen [2019] (Ref 7)	Metco 204F	HOSP	– 15 + 45	Metco-SimplexPro (9 mm)	Pre-heated up to 170 °C with plasma
	Metco 233B	Agglomerated & sintered	– 22 + 45		
	Metco 214A	Fused & crushed	– 11 + 45		
	Metco 204G	HOSP	– 11 + 125		
Shinde [2020] (Ref 13)	Saint Gobain 204F	HOSP	– 10 + 45	Metco-F4 MB (8 mm)	Pre-heated with plasma
This study	Metco 204F	HOSP	– 44 + 16	GTV F6 (6 mm)	Without pre-heated
	Amperit 825	Fused & crushed	– 60 + 25		

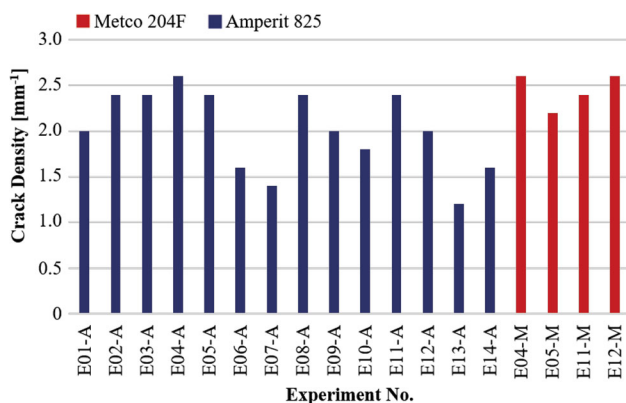


Fig. 11 Crack density of experiments between E01-A and E14-A, E04-M, E05-M, E11-M, and E12-M

a desirable microstructure. When the same spray process parameters are applied with the HOSP, it is observed that the coating thickness per pass is thinner, and nevertheless, the horizontal cracks are longer. The remarkable differences between these two powders are the powder particle

size, the morphology of the powder, and different amounts of cubic and tetragonal phases, which are caused by manufacturing methods.

Conclusions

In this study, the optimization of segmented thermal barrier coatings (s-TBCs) for the application of stationary gas turbines by atmospheric plasma spraying (APS) has been carried out. The effect of individual spray process parameters has been shown. The main factor for vertical crack induction is the process temperature or more specifically the substrate and plasma temperature as well as the coating thickness per pass. Moreover, it is determined that the powder characteristic significantly affects the formation of horizontal (branching) cracks, yet has little impact on the vertical (segmentation) crack density. For further investigation, the coatings will be proceeded with other plasma properties, for example, using another type of plasma torch

Fig. 12 Effect of coating thickness (CT) per pass on the segmented microstructure of Amperit 825

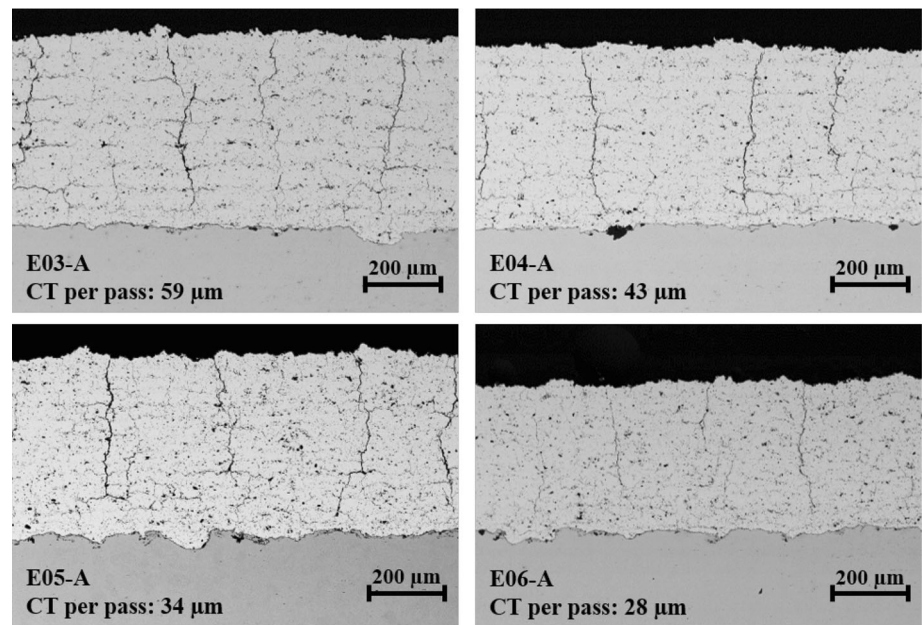
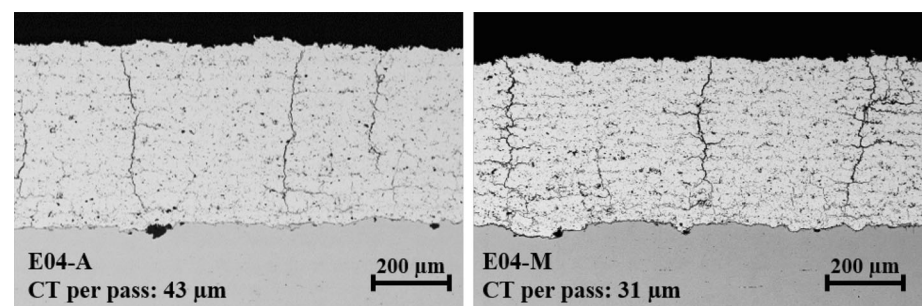


Fig. 13 Effect of powder type on the segmented microstructure with the same process parameters (A: fused & crushed, M: HOSP)



(3 anodes + 1 cathode) in order to optimize the segmented microstructure.

Acknowledgments This work takes place in the context of the project Maintenance, Repair & Overhaul (MRO) inside the industry and science campus Werner-von-Siemens Centre and is financed by the European Regional Development Fund (ERDF).

Funding Open Access funding enabled and organized by Projekt DEAL.

Open Access This article is licensed under a Creative Commons Attribution 4.0 International License, which permits use, sharing, adaptation, distribution and reproduction in any medium or format, as long as you give appropriate credit to the original author(s) and the source, provide a link to the Creative Commons licence, and indicate if changes were made. The images or other third party material in this article are included in the article's Creative Commons licence, unless indicated otherwise in a credit line to the material. If material is not included in the article's Creative Commons licence and your intended use is not permitted by statutory regulation or exceeds the

permitted use, you will need to obtain permission directly from the copyright holder. To view a copy of this licence, visit <http://creativecommons.org/licenses/by/4.0/>.

References

1. E. Bakan, D. E. Mack, G. Mauer, R. Vaßen, J. Lamon, and N. P. Padture, High-temperature materials for power generation in gas turbines, *Advanced Ceramics for Energy Conversion and Storage*, Elsevier Series on *Advanced Ceramic Materials*, 2020, pp 3-62
2. S. Bose, Thermal Barrier Coatings (TBCs), *High Temperature Coatings*, 2nd ed. (Butterworth-Heinemann an imprint of Elsevier, 2018), pp 199-299
3. S. Stecura, Optimization of the NiCrAl-Y/ZrO-Y2O3 Thermal Barrier System, National Aeronautics and Space Administration (NASA), 1985, 87 Annual Meeting of the American Ceramic Society
4. P.G. Lashmi, P.V. Ananthapadmanabhan, G. Unnikrishnan, and S.T. Aruna, Present Status and Future Prospects of Plasma Sprayed Multilayered Thermal Barrier Coating Systems, *J. Eur. Ceram. Soc.*, 2020, **40**, p 2731-3745.

5. H. Guo, R. Yao, and L. Zhou, *Chapter 8: Plasma-Sprayed Thermal Barrier Coatings with Segmentation Cracks*, Woodhead Publishing Series in Metals and Surface Engineering, Thermal Barrier Coatings, 2011, p 161-174
6. C. Li, G. Yang, and Ö. Altun, *Chapter 6: Thermal Spray Coatings for Aeronautical and Aerospace Applications*, CRC Press, Aerospace Materials Handbook, 2013, p 281-358
7. D. Chen, R. Rocchio-Heller, and C. Dambra, Segmented Thermal Barrier Coatings for ID and OD Components Using the SimplexPro Plasma Torch, *J. Therm. Spray Technol.*, 2019, **28**, p 1664-1673.
8. H.B. Guo, S. Kuroda, and H. Murakami, Segmented Thermal Barrier Coatings Produced by Atmospheric Plasma Spraying Hollow Powders, *Thin Solid Films*, 2005, **506-507**, p 136-139.
9. J.R. Nicholls, K.J. Lawson, A. Johnstone, and D.S. Rickerby, Methods to Reduce the Thermal Conductivity of EB-PVD TBCs, *Surf. Coat. Technol.*, 2002, **151-152**, p 383-391.
10. D. Chen, C. Dambra, and M. Dorfman, Process and Properties of Dense and Porous Vertically-Cracked Yttria Stabilized Zirconia Thermal Barrier Coatings, *Surf. Coat. Technol.*, 2020, **404**, p 126467.
11. The rotor of an SGT5-4000F gas turbine during assembly, <https://press.assets.siemens-energy.com/content/siemens-energy/press/ui/en/search.html#/asset/sid:80c8001f-41b0-4d10-8ec3-6f4fd6353c5d>, Accessed 27 Oct 2022
12. T. A. Taylor, US Patent No. 5073433, Thermal barrier coating for substrates and process for producing it, 1991
13. S.V. Shinde, E.J.V. Gildersleeve, C.A. Johnson, and S. Sampath, Segmentation Crack Formation Dynamics During air Plasma Spraying of Zirconia, *Acta Mater.*, 2020, **183**, p 196-206.
14. H.B. Guo, R. Vaßen, and D. Stöver, Atmospheric Plasma Sprayed Thick Thermal Barrier Coatings with High Segmentation Crack Density, *Surf. Coat. Technol.*, 2004, **186**(3), p 353-363.
15. M. Karger, R. Vaßen, and D. Stöver, Atmospheric Plasma Sprayed Thermal Barrier Coatings with High Segmentation Crack Densities: Spraying Process, Microstructure and Thermal Cycling Behavior, *Surf. Coat. Technol.*, 2011, **206**, p 16-23.
16. Höganäs GmbH, Thermal spray powders, https://www.hoganas.com/globalassets/download-media/sharepoint/brochures-and-data-sheets—all-documents/surface-coating_thermal-spray-powders_2438hog.pdf, 2019, Accessed 21 Aug 2022
17. Oerlikon Metco GmbH, Werkstoffe für das Thermische Spritzen, https://oerlikon.com/ecoma/files/TS_MaterialGuide_DE_2017_04.pdf?download=1, 2017, Accessed 21 Aug 2022 (in German)
18. P. Scherrer, Bestimmung der inneren Struktur und der Größe von Kolloidteilchen mittels Röntgenstrahlen, *Kolloidchemie Ein Lehrbuch*, (1912), 387-409, (in German)
19. J. Ilavsky and J.K. Stalicka, Phase Composition and its Changes During Annealing of Plasma-Sprayed YSZ, *Surf. Coat. Technol.*, 2000, **127**, p 120-129.
20. T. Götsch, W. Wallisch, M. Stöger-Pollach et al., From Zirconia to Yttria: Sampling the YSZ Phase Diagram Using Sputter-Deposited Thin Films, *AIP Adv.*, 2016, **6**, p 1-20.
21. F. Zhang, H. Reveron, B.C. Spies, B.V. Meerbeek, and J. Chevalier, Trade-off Between Fracture Resistance and Translucency of Zirconia and Lithium-Disilicate Glass Ceramics for Monolithic Restorations, *Acta Biomater.*, 2019, **91**, p 24-34.
22. X. Mao, H. Shan, J. Song, Y. Bai, J. Yuc, and B. Ding, Brittle-Flexible-Brittle Transition in Nanocrystalline Zirconia Nanofibrous Membranes, *R. Soc. Chem.*, 2016, **18**, p 1139-1146.
23. L. Pawlowski, *The Science and Engineering of Thermal Spray Coatings*, 2nd edn. (John Wiley & Sons, Ltd, 2008), pp. 168-180
24. D. Schwingel, R. Taylor, T. Haubold, J. Wigren, and C. Gualco, Mechanical and Thermophysical Properties of Thick PYSZ Thermal Barrier Coatings: Correlation with Microstructure and Spraying Parameters, *Surf. Coat. Technol.*, 1998, **108-109**, p 99-106.

Publisher's Note Springer Nature remains neutral with regard to jurisdictional claims in published maps and institutional affiliations.